Title

Hyperpolarized 13C MR metabolic imaging can detect neuroinflammation in vivo in a multiple sclerosis murine model

Permalink

https://escholarship.org/uc/item/5f9754jq

Journal

Proceedings of the National Academy of Sciences of the United States of America, 114(33)

ISSN

0027-8424

Authors

Guglielmetti, Caroline
Najac, Chloé
Didonna, Alessandro
et al.

Publication Date

2017-08-15

DOI

10.1073/pnas.1613345114

Peer reviewed

Hyperpolarized ^{13}C MR metabolic imaging can detect neuroinflammation in vivo in a multiple sclerosis murine model

Caroline Guglielmetti[a,b], Chloé Najac[c], Alessandro Didonna[d], Annemie Van der Linden[b], Sabrina M. Ronen[c,e], and Myriam M. Chaumeil[a,c,1]

[a]Department of Physical Therapy and Rehabilitation Science, University of California, San Francisco, CA 94143; [b]Bio-Imaging Laboratory, Department of Pharmaceutical, Veterinary and Biomedical Sciences, University of Antwerp, 2000 Antwerp, Belgium; [c]Surbeck Laboratory of Advanced Imaging, Department of Radiology and Biomedical Imaging, University of California, San Francisco, CA 94143; [d]Department of Neurology, University of California, San Francisco, CA 94143; and [e]Brain Tumor Research Center, University of California, San Francisco, CA 94143

Proinflammatory mononuclear phagocytes (MPs) play a crucial role in the progression of multiple sclerosis (MS) and other neurodegenerative diseases. Despite advances in neuroimaging, there are currently limited available methods enabling noninvasive detection of MPs in vivo. Interestingly, upon activation and subsequent differentiation toward a proinflammatory phenotype MPs undergo metabolic reprogramming that results in increased glycolysis and production of lactate. Hyperpolarized (HP) ^{13}C magnetic resonance spectroscopic imaging (MRSI) is a clinically translatable imaging method that allows noninvasive monitoring of metabolic pathways in real time. This method has proven highly useful to monitor the Warburg effect in cancer, through MR detection of increased HP [1-^{13}C]pyruvate-to-lactate conversion. However, to date, this method has never been applied to the study of neuroinflammation. Here, we questioned the potential of ^{13}C MRSI of HP [1-^{13}C]pyruvate to monitor the presence of neuroinflammatory lesions in vivo in the cuprizone mouse model of MS. First, we demonstrated that ^{13}C MRSI could detect a significant increase in HP [1-^{13}C]pyruvate-to-lactate conversion, which was associated with a high density of proinflammatory MPs. We further demonstrated that the increase in HP [1-^{13}C]lactate was likely mediated by pyruvate dehydrogenase kinase 1 up-regulation in activated MPs, resulting in regional pyruvate dehydrogenase inhibition. Altogether, our results demonstrate a potential for ^{13}C MRSI of HP [1-^{13}C]pyruvate as a neuroimaging method for assessment of inflammatory lesions. This approach could prove useful not only in MS but also in other neurological diseases presenting inflammatory components.

hyperpolarized ^{13}C MR spectroscopy | multiple sclerosis | neuroinflammation | metabolism | macrophages

Multiple sclerosis (MS) is a multifaceted disorder of the CNS and is one of the most common causes of neurological disability in young adults (1, 2). Cortical and white-matter demyelination occurs early in MS pathogenesis and has been associated with disease progression and subsequent cognitive impairment (3). In the vast majority of cases, demyelinating lesions present a high inflammatory component, with elevated density of activated microglia/macrophages (mononuclear phagocytes, MPs) (4–6). Importantly, evidence suggests that proinflammatory MPs are one of the most abundant sources of reactive oxygen species (7), which mediate demyelination and axonal injury (8). Due to their central role in MS pathogenesis, noninvasive imaging of proinflammatory MPs would be of high importance for monitoring progression and response to antiinflammatory therapeutic approaches.

Several recent studies have demonstrated that, upon activation and differentiation toward a proinflammatory phenotype, MPs undergo metabolic reprogramming toward enhanced glucose uptake and increased glycolysis (9–14). As for the Warburg effect observed in cancer cells, this augmented glycolysis takes place under aerobic conditions and results in the majority of pyruvate being converted to

lactate (15). However, the molecular mechanisms by which aerobic glycolysis is increased in MPs are still not fully understood. Novel studies have uncovered a potential underlying mechanism, showing pyruvate dehydrogenase kinase 1 (PDK1) up-regulation in proinflammatory MPs (13, 16). Because PDK1 inhibits pyruvate dehydrogenase (PDH), the enzyme that controls pyruvate entrance into the Krebs cycle, PDK1 up-regulation in activated MPs results in increased pyruvate-to-lactate conversion (12, 17, 18). In line with these observations, lactate has long been suggested as an imaging marker of neuroinflammation in the clinic. A few studies on MS patients have used ^{1}H magnetic resonance spectroscopy (MRS)/ MRS imaging (MRSI) approaches and detected increased levels of ^{1}H lactate in gadolinium-enhancing lesions (19, 20) as well as in the cerebrospinal fluid of patients with such active lesions (21–24).

Over the last decade, dissolution dynamic nuclear polarization coupled with ^{13}C MRSI has developed as a metabolic imaging approach of high potential (25, 26). Through increase in the MR-detectable signal of ^{13}C compounds by up to 50,000 [so-called hyperpolarized (HP) probes] this methodology has enabled the noninvasive monitoring of several metabolic reactions in vivo (27–32). In particular, in the context of cancer, HP ^{13}C MRSI has been shown to improve the noninvasive detection of

---

Significance

Cells from the innate immune system, namely microglia and macrophages (mononuclear phagocytes, MPs), play a central role in the progression of neurological disorders such as multiple sclerosis. Such cells can contribute to lesion formations (proinflammatory) or participate in remyelinating processes (neuroprotective). When differentiated to a proinflammatory phenotype, MPs experience metabolic reprogramming leading to increased glycolysis and production of lactate. In this study we showed that a new metabolic imaging method, namely ^{13}C magnetic resonance spectroscopic imaging (MRSI) of hyperpolarized pyruvate, can detect increased lactate production from proinflammatory MPs, a mechanism mediated by pyruvate dehydrogenase kinase 1 upregulation, in a preclinical model of multiple sclerosis. These findings validate the potential of ^{13}C MRSI of hyperpolarized pyruvate for in vivo detection of neuroinflammation.

cancerous lesions through the monitoring of the increased HP [1-^{13}C]pyruvate-to-lactate conversion, not only in preclinical cancer models but also in the clinical setting (33).

To date, ^{13}C MRSI of HP [1-^{13}C]pyruvate has only been applied to investigate inflammation in three studies: a rat model of radiation-induced lung injury (34), a mouse model of inflammatory arthritis (35), and a mouse model of acute liver injury (36). In all three cases, ^{13}C MRSI of HP [1-^{13}C]pyruvate was capable of detecting an in-crease in the HP [1-^{13}C]lactate-to-pyruvate ratio in the inflammatory region, which was associated with an increased number of macro-phages as detected by H&E staining. These three studies are in line with the literature of increased glycolysis in activated MPs. However, to date, no studies have reported the use of ^{13}C MRSI of HP [1-^{13}C]pyruvate to study neuroinflammation, and underlying biochemical mechanisms linked to increased HP [1-^{13}C]lactate production in inflammatory models are still lacking.
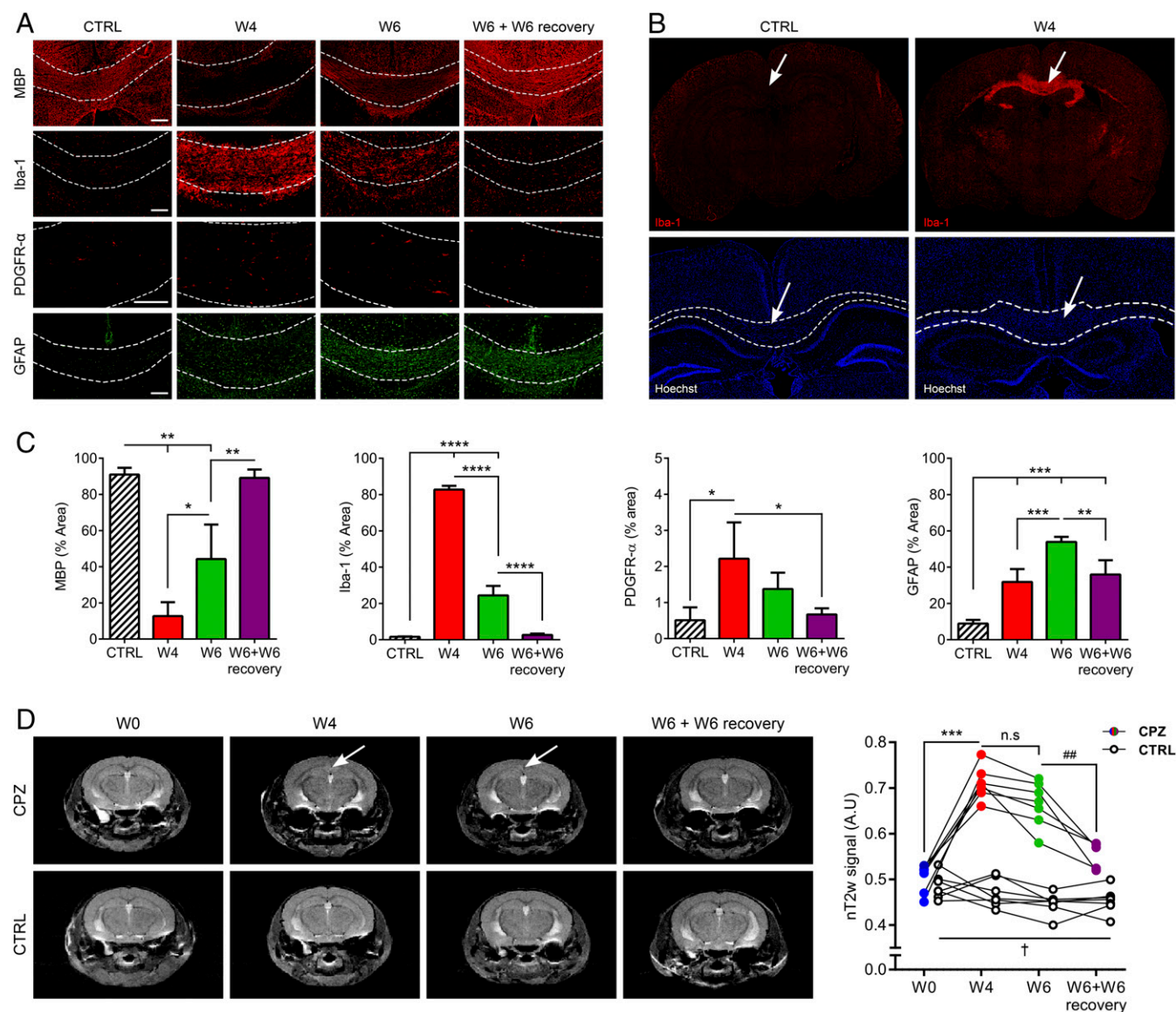

Fig. 1. Histological and MRI characterization of CPZ mice. (A) Myelin (MBP), microglia/macrophages (Iba-1, MPs), oligodendrocyte progenitor cells (OPCs, PDGFR-α), and astrocytes (GFAP) staining of the corpus callosum (dashed lines) prior to (W0) and following CPZ diet (W4, W6), and after recovery (W6 + W6 recovery). (Scale bar: 100 μm.) (B) Immunofluorescence staining illustrates the massive cell infiltration of activated MPs (Iba-1; nuclear staining Hoechst) in the corpus cal-losum (white arrows) at W4 of CPZ compared with CTRL. (Magnification: 10×; scaling per pixel, 0.645 μm × 0.645 μm.) (C) Quantitative analyses of the corpus callosum confirm demyelination (MBP, $P < 0.0001$) and maximal microgliosis (Iba-1, $P < 0.0001$) after W4 of CPZ. Remyelination and decreased MP levels are observed following W6 of CPZ diet ($P = 0.0285$ and $P < 0.0001$, respectively). Myelin and MP levels return to CTRL levels at W6 + W6 recovery. OPCs (PDGFR-α) accumulate at W4 of CPZ ($P = 0.0299$) and return to CTRL levels at W6 + W6 recovery ($P = 0.0479$). Astrocyte (GFAP) staining quantification shows highest astrogliosis after W6 of CPZ ($P < 0.0001$), which persists after the recovery period ($P < 0.0001$) ($n = 3–5$ mice per group). All values are reported as mean ± SD. (D) T_2-weighted MR images show hyperintensity in the corpus callosum at W4 and W6 of CPZ diet (white arrows). Corresponding nT$_2$w values increased at W4 and W6 of CPZ ($P ≤ 0.0003$), in line with demyelination and neuroinflammation at these time points. At W6 + W6 recovery, hypointense contrast can be observed in the corpus callosum, resulting in a decrease of nT$_2$w toward CTRL values ($P = 0.0011$), indicating remyelination and decreased neuroinflammation ($n = 5–7$ mice per group). In the CTRL group, the nT$_2$w values decreased over time, reflecting myelination of the corpus callosum in young adult mice. All values are reported as mean ± SD (one-way ANOVA and two-Way ANOVA, Tukey HSD post hoc test *$P < 0.05$, **$P < 0.01$, ***$P < 0.001$, ****$P < 0.0001$; unpaired t test ##$P < 0.01$; repeated measures ANOVA †$P < 0.05$). n.s., not significant. A.U., arbitrary unit.

In this context, we questioned whether ^{13}C MRSI of HP [1-^{13}C]pyruvate could monitor the presence of activated MPs in neuroinflammatory lesions in the mouse brain. We conducted a longitudinal study of the toxin-induced cuprizone (CPZ) mouse model, a well-established MS model characterized by high spatial and temporal reproducibility of neuroinflammatory lesions (37, 38). Our results demonstrated a significant increase in HP [1-^{13}C]pyruvate-to-lactate conversion in the corpus callosum of CPZ mice as detected by ^{13}C MRSI at 14.1 T. Using immunofluorescence, we then showed that increased HP [1-^{13}C]lactate production was associated with a high density of activated proinflammatory MPs that overexpressed PDK1. We further showed that the enzymatic activity of PDH was significantly down-regulated in neuroinflammatory lesions, likely due to PDK1 up-regulation, thus providing a putative mechanism for the increased HP [1-^{13}C]lactate production observed by ^{13}C MRSI. Finally, using transgenic mice exhibiting an impaired microglial function following CPZ diet, we further confirmed that the increased HP [1-^{13}C]lactate conversion was primarily driven by the presence of activated MPs in cerebral lesions.

Results

Histological and MRI Characterization of the CPZ Mouse Model.
In the initial part of this study our goal was twofold. First, we wanted to confirm that, in our hands, the CPZ mouse model was behaving as previously described in terms of spatial and temporal distribution of lesions (37, 39–42). Next, we evaluated the potential of T_2-weighted MRI at high field strength (14.1 T) to detect cerebral lesions in CPZ mice.

As shown in Fig. 1 A–C, histological analyses confirmed our CPZ model reproduced findings reported in the literature, presenting demyelination (myelin basic protein, MBP), recruitment of MPs (ionized calcium-binding adapter molecule 1, Iba-1) into the corpus callosum, accumulation of oligodendrocytes progenitor cells (OPCs) (PDGF receptor alpha chain, PDGFR-α), and astrogliosis (glial fibrillary acid protein, GFAP). After 4 wk (W4) of CPZ diet, myelin content was significantly decreased by $86 \pm 9\%$ of control (CTRL) level ($P < 0.0001$) and MP number significantly increased by a dramatic $5,230 \pm 762\%$ ($P < 0.0001$). This massive infiltration of MPs after W4 of CPZ was mainly restricted to the corpus callosum and surrounded the dorsal hippocampal formation (Fig. 1B). In contrast, at 6 wk (W6) of CPZ diet, remyelination reached $51 \pm 23\%$ of the CTRL level and MPs were strongly diminished to $30 \pm 6\%$ of W4 ($P = 0.0285$ and $P < 0.0001$, respectively). At the end of the recovery period both myelin content and MP numbers reached CTRL levels. In addition, significant accumulation of OPCs (PDGFR-α) into the corpus callosum was observed at W4 of CPZ ($668 \pm 500\%$, $P = 0.0299$) and was later followed by a decrease to CTRL levels once remyelination had occurred at W6 + W6 recovery ($P = 0.0479$). Astrogliosis, as demonstrated by an increase of GFAP, was present after W4 of CPZ ($362 \pm 200\%$, $P = 0.0004$), peaked after W6 of CPZ ($645 \pm 200\%$, $P < 0.0001$), and remained elevated after the recovery period, eventually forming a glial scar ($410 \pm 225\%$, $P < 0.0001$). When looking at all cell types it is important to note that the maximum level of MP staining reached $83 \pm 2\%$ area at W4 (Iba-1+), whereas the maximum level of astrocytes reached $54 \pm 3\%$ area at W6 (GFAP+), and OPC staining was maximum at W4 with $2.2 \pm 1\%$ area (PDGFR-α+).

On T_2-weighted MR images, hyperintensity could be observed in the corpus callosum of CPZ mice following W4 and W6 of CPZ administration (Fig. 1D, arrows). Upon quantification, our results showed that normalized T_2-weighted (nT_2w) signals from the corpus callosum were significantly different between CPZ and CTRL groups ($P < 0.0001$ for group and time effects and for group and time interaction). The nT_2w signals from the corpus callosum of CPZ-treated mice were significantly higher than those from the CTRL mice at any time point following CPZ diet ($P < 0.0001$ for W4, W6, and W6 + W6 recovery). Furthermore, nT_2w signals from

CPZ mice were increased by $42 \pm 13\%$ after W4, $33 \pm 16\%$ after W6 of CPZ diet, and $12 \pm 9\%$ after recovery compared with W0 ($P < 0.0001$ for W4 and W6 and $P = 0.0174$ for W6 + W6 recovery). However, no significant difference in nT_2w signal values could be observed between W4 and W6 CPZ ($P = 0.0562$), despite the differences in underlying pathophysiological events observed at these two time points. In the CTRL group, nT_2w signals significantly decreased over time ($P = 0.0269$), likely reflecting myelination of the corpus callosum in young adult mice (40, 43).

Increased Production of HP [1-^{13}C]Lactate Following MP Activation in CPZ-Induced Lesions.
Next, we evaluated the potential of ^{13}C MRSI of HP [1-^{13}C]pyruvate to monitor the presence of proinflammatory MPs. To do so, as shown in Fig. S1, MR experiments were performed at W0, W4, and W6 of CPZ diet and W6 of CPZ diet followed by W6 of standard rodent chow.

As shown in Fig. 2 A and B, the level of HP [1-^{13}C]pyruvate detected in the corpus callosum voxel remained stable over time in CTRL and CPZ mice. In contrast, a significant increase of HP [1-^{13}C]lactate was observed in the corpus callosum region following W4 of CPZ administration (Fig. 2A). Upon full quantification, our results showed that the ratio of HP [1-^{13}C]lactate to pyruvate was significantly different between CPZ and CTRL groups over time ($P = 0.0014$ for group effect, $P = 0.045$ for time effect, and $P = 0.0004$ for group and time interaction). Specifically, when comparing CTRL and CPZ groups, the HP [1-^{13}C]lactate-to-pyruvate ratio was more than threefold higher in the corpus callosum of CPZ mice after W4 of CPZ diet compared with age-matched CTRL ($P = 0.0006$), a time point that corresponds to the highest level of activated proinflammatory MPs (Fig. 2C). At that time point, T_1-weighted MRI after injection of a gadolinium-based contrast agent showed similar signal enhancement in the corpus callosum of CTRL and W4 CPZ mice (Fig. S2). Next, longitudinal evaluation revealed a significant increase of the HP [1-^{13}C]lactate-to-pyruvate ratio after W4 of CPZ compared with W0 ($96 \pm 74\%$ of W0, $P = 0.0002$), followed by a significant decrease after W6 of CPZ ($42 \pm 59\%$ of W4, $P = 0.0194$), when MPs numbers are strongly decreased and remyelination is occurring. By the end of the recovery period, the HP [1-^{13}C]lactate-to-pyruvate ratio remained significantly decreased compared with W4 CPZ ($131 \pm 24\%$ of W4, $P = 0.0346$) and was no longer significantly different from W0 values ($P = 0.2005$) (Fig. 2D). The two animals that were not imaged at W6 + W6 were excluded from the statistical analysis between W4 and W6 + W6.

As shown on the heat maps of HP [1-^{13}C]lactate-to-pyruvate ratio, the increase in HP [1-^{13}C]lactate production was localized to the corpus callosum voxel only, in line with the high level of activated MPs in that cerebral region (Fig. 3A). To further assess the specificity of ^{13}C MRSI of HP [1-^{13}C]pyruvate to detect proinflammatory MPs, we examined the levels of HP [1-^{13}C]lactate and HP [1-^{13}C]pyruvate in a thalamic voxel (dark blue) as well as in an heterogeneous neck voxel outside the brain (light blue), regions that do not display a large recruitment, proliferation, and activation of MPs (Fig. 3B). In line with the HP [1-^{13}C]lactate maps, the grid of the HP ^{13}C spectra showed an increased HP [1-^{13}C]lactate in the region that contains the demyelinated and inflamed corpus callosum (Fig. 3B, red) but not in the adjacent brain regions (Fig. 3B, dark and light blue). In both the thalamic and the neck region the level of HP [1-^{13}C]pyruvate remained stable over time for both CPZ and CTRL groups (Fig. 3 C and D) and the HP [1-^{13}C]lactate-to-pyruvate ratio did not significantly differ between CPZ and age-matched CTRL (Fig. 3 E and F). T_1-weighted postcontrast also showed no differences in thalamus kinetic parameters between CTRL and W4 CPZ mice (Fig. S2).

The Increase in HP [1-^{13}C]Lactate Signal Is Associated with Up-Regulation of PDK1 in Activated MPs and Decreased PDH Activity in the Corpus Callosum.
We performed immunofluorescence for PDK1, a protein that inhibits PDH and thus controls pyruvate
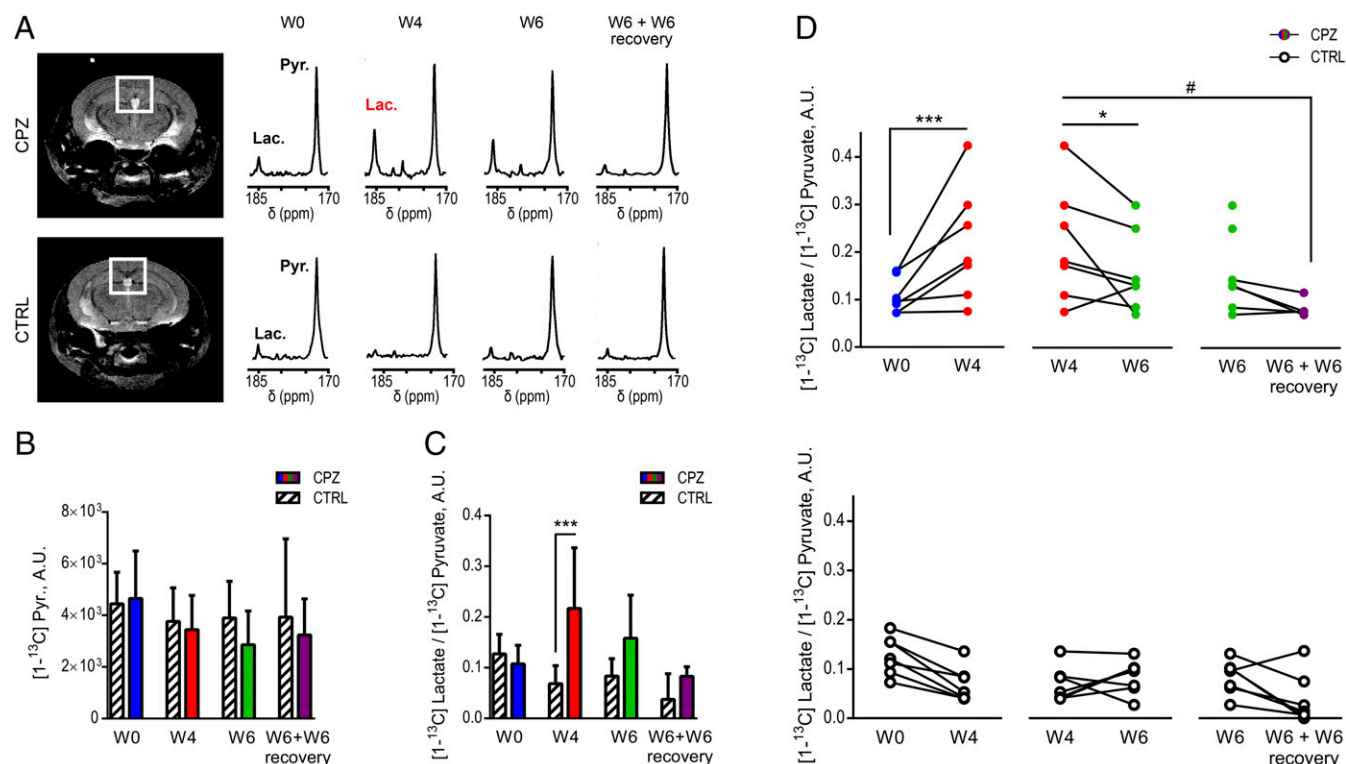
Fig. 2. Increased production of HP [1-^{13}C]lactate in CPZ-induced lesions. (*A*) HP ^{13}C spectra from the corpus callosum (white voxels) show an increased HP [1-^{13}C]lactate production after W4 of CPZ diet. (*B*) HP [1-^{13}C]pyruvate delivery is unchanged between CTRL and CPZ at any time point of interest. (*C*) When comparing CPZ and CTRL groups, the HP [1-^{13}C]lactate-to-pyruvate ratios are significantly increased after W4 of CPZ diet ($315 \pm 338\%$, $P = 0.0006$). (*D*) Longitudinal analyses of the HP [1-^{13}C]lactate-to-pyruvate ratios between W0 (blue), W4 CPZ (red), W6 CPZ (green), and W6 + W6 recovery (purple) show a significant increase at W4 ($96 \pm 74\%$ of W0, $P = 0.0002$) followed by a decrease at W6 and W6 + W6 recovery ($P = 0.0194$ and $P = 0.0346$, respectively). The two animals that were not imaged at W6 + W6 were excluded from the statistical analysis between W4 and W6 + W6. HP [1-^{13}C]lactate-to-pyruvate ratios of the CTRL mice (open circles) did not show any significant differences over time ($n = 5$–7 mice per group). All values are reported as mean $\pm$ SD (two-way ANOVA, Tukey HSD post hoc test *$P < 0.05$, ***$P < 0.001$, ****$P < 0.0001$; unpaired t test #$P < 0.05$). A.U., arbitrary unit; Lac, lactate; Pyr, pyruvate.

entrance into the Krebs cycle. Interestingly, we demonstrated a significant up-regulation of PDK1 (PDK1+) in activated MPs (Iba-1+) following W4 of CPZ administration in the corpus callosum, but not in other brain regions (cortex and thalamus), as shown in Fig. 4*A* and Fig. S3. Whereas only $12 \pm 7\%$ of Iba-1+ were also PDK1+ at W0, this number significantly increased at W4 ($87 \pm 7\%$ of MPs are PDK1+/Iba-1+, $P < 0.0001$) and W6 after CPZ diet ($82 \pm 8\%$ of MPs are PDK1+/Iba-1+, $P = 0.001$), in line with a higher density of activated MPs at these time points. Cellular colocalization of PDK1 and Iba-1 was further confirmed by confocal microscopy (Fig. 4*B*). Importantly, GFAP/PDK1 and PDGFR-α/PDK1 costaining revealed that neither astrocytes nor OPCs overexpressed PDK1 at any time point (Fig. 4*B* and Fig. S3), providing additional evidence that these other cell types do not play a major role in the HP [1-^{13}C]lactate signal increase at W4 of CPZ.

Next, we wanted to investigate whether PDK1 up-regulation by Iba-1 MPs was associated with a modulation in the activity of its downstream target PDH. As shown in Fig. 4*C*, PDH activity was significantly decreased in the corpus callosum of W4 mice compared with W0 ($57 \pm 15\%$ decrease, $P = 0.0026$), but not in the thalamus (Fig. S3), suggesting a regional effect of Iba-1+ MPs PDK1 up-regulation on PDH activity. Further in line with this putative link, after W6 of CPZ and after the recovery period the number of PDK1+/Iba-1+ MPs present in the corpus callosum significantly decreased and PDH activity no longer differed from CTRL levels. We also investigated lactate dehydrogenase A (LDH-A), the isoenzyme that converts pyruvate to lactate and is overexpressed in most cancer types. Unlike in cancer, we did not observe an up-regulation

of LDH-A staining in the corpus callosum (Fig. S3) or a change in LDH-A activity at any time point (Fig. 4*D*), thus ruling out overexpression of this enzyme as a main player in the observed increased HP [1-^{13}C]lactate production at W4 CPZ.

Finally, we measured serum lactate levels in CPZ and CTRL mice at all time points. As shown in Fig. 4*E*, serum lactate levels were significantly increased at W4 and W6 of CPZ ($161 \pm 62\%$ W4 $P = 0.0014$; $166 \pm 48\%$ W6 $P = 0.0007$) and returned to CTRL levels by the end of the recovery period ($P = 0.0024$), confirming the systemic effect of CPZ diet (38, 44, 45).

HP [1-^{13}C]Lactate Levels Are Not Increased in the Corpus Callosum of CX$_3$CR1$^{GFP/GFP}$ Transgenic Mice Harboring Microglial Activation Deficiency, Suggesting a Central Role of MPs to the Detected HP [1-^{13}C]Lactate Signal. To confirm that the production of HP [1-^{13}C]lactate was driven by the presence of MPs into the corpus callosum following CPZ diet, we studied CX$_3$CR1$^{GFP/GFP}$ mice, which exhibit highly reduced or absent microgliosis, astrogliosis, and demyelination at W4 of CPZ diet, as previously described (39). In these mice, the CX$_3$CR1 receptor, which is highly expressed in microglia, is replaced by GFP, allowing one to easily monitor microglia levels by immunofluorescence (46).

As shown in Fig. 5*A*, CPZ diet did not induce hyperintensities characteristic of demyelination and inflammation on T$_2$-weighted MR images in the corpus callosum of CX$_3$CR1$^{GFP/GFP}$ mice. Quantitative analyses of the nT$_2$w values from the corpus callosum showed that nT$_2$w were significantly decreased at W4 in CPZ and CTRL CX$_3$CR1$^{GFP/GFP}$, as well as in CTRL nontransgenic mice, reflecting normal myelination throughout development (40, 43). In contrast to nontransgenic CPZ mice, however, no differences in T$_2$w
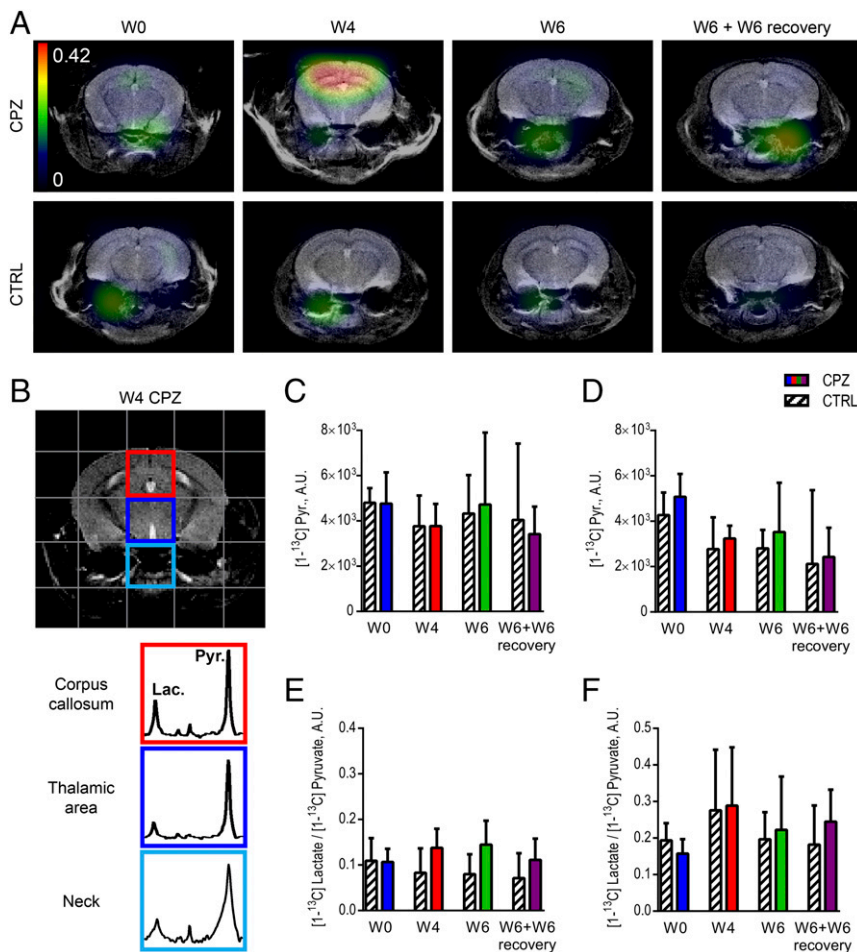
Fig. 3. Increased HP [1-^{13}C]lactate-to-pyruvate ratio is restricted to the inflamed and demyelinated corpus callosum. (*A*) HP [1-^{13}C]lactate-to-pyruvate ratio heat maps display an increased HP [1-^{13}C]lactate production after W4 of CPZ diet in the corpus callosum only. (*B*) T$_2$-weighted image overlaid with the grid used for HP ^{13}C MR acquisition is shown for a W4 CPZ mouse. The corresponding sum of dynamic spectra is presented. Increased HP [1-^{13}C]lactate can be observed in the voxel containing the corpus callosum (red) but not in a voxel containing the thalamic region (dark blue) or in a nonbrain voxel located beneath the brain (neck voxel, light blue). (*C* and *D*) HP [1-^{13}C]pyruvate delivery as well as (*E* and *F*) HP [1-^{13}C]lactate-to-pyruvate ratios were not significantly different between CTRL and CPZ groups over time in the thalamic and neck region (*n* = 5–7 mice per group; *C* and *E* thalamus and *D* and *F* neck). All values are reported as mean ± SD. A.U., arbitrary unit.

MR contrast could be detected between CTRL and CPZ groups at W0 or W4. Immunofluorescence analyses further confirmed the absence of microgliosis (CX$_3$CR1$^{GFP/GFP}$ labeled microglia), cell infiltration, demyelination, and astrogliosis (Fig. S4) in the corpus callosum of CX$_3$CR1$^{GFP/GFP}$ mice, despite W4 of CPZ diet, and in line with previous reports (37, 39).

Importantly, PDH (Fig. 5*B*) and LDH-A (Fig. 5*C*) activities measured from the corpus callosum of CX$_3$CR1$^{GFP/GFP}$ mice were not significantly different between CTRL and CPZ animals at W4. As expected however, and similar to the nontransgenic model, the serum lactate levels (Fig. 5*D*) were increased by 173 ± 79% (*P* = 0.0079) in CX$_3$CR1$^{GFP/GFP}$ mice after W4 of CPZ diet compared with CTRL mice, confirming the systemic effect of the CPZ diet.

We then performed HP ^{13}C MRSI to further confirm that increased HP [1-^{13}C]lactate was associated with the presence of proinflammatory MPs. HP ^{13}C spectra acquired in the corpus callosum of CX$_3$CR1$^{GFP/GFP}$ mice show no evident differences between CTRL and CPZ groups (Fig. 5*E*). Spectra quantification showed that, in contrast to the nontransgenic mice, HP [1-^{13}C]lactate-to-pyruvate ratios for the corpus callosum were similar between CTRL and CPZ groups at W4 of CPZ diet, in line with the absence of MP activation and infiltration in this transgenic model (Fig. 5*F*). Similarly, HP [1-^{13}C]lactate-to-pyruvate ratios from the thalamic area (Fig. 5*G*) and the neck (Fig. 5*H*) were not

significantly different between CTRL and CPZ groups at W4. HP [1-^{13}C]pyruvate delivery was also unchanged in all regions (Fig. S4).

PDK1 Is Up-Regulated in Activated MPs in Experimental Autoimmune Encephalomyelitis Lesions. Finally, to further assess the validity of our findings, we investigated whether the up-regulation of PDK1 by MPs was also present in demyelinated lesions in another animal model for MS. For this, we performed immunofluorescence analyses on tissues from experimental autoimmune encephalomyelitis (EAE) mice. Most neuroinflammatory lesions were found in the spinal cord and brainstem in close vicinity to blood vessels. We found that 45 ± 8% of MPs present in the EAE group expressed PDK1 in the spinal cord (Fig. 6 *A*–*C*), 28 ± 8% in the brainstem, and 25 ± 7% in the cerebellar white matter (Fig. 6 *B* and *C*), whereas the level of detection for PDK1 was below detection for age-matched CTRL (Fig. 6*A*).

Discussion

In this study we applied a metabolic imaging method, ^{13}C MRSI of HP [1-^{13}C]pyruvate, to the longitudinal study of the CPZ model of MS. HP [1-^{13}C]pyruvate-to-lactate conversion increased in the corpus callosum of CPZ mice at W4 of CPZ diet, a time point presenting the highest density of proinflammatory MPs. In contrast, in knockout CX$_3$CR1$^{GFP/GFP}$ animals with low
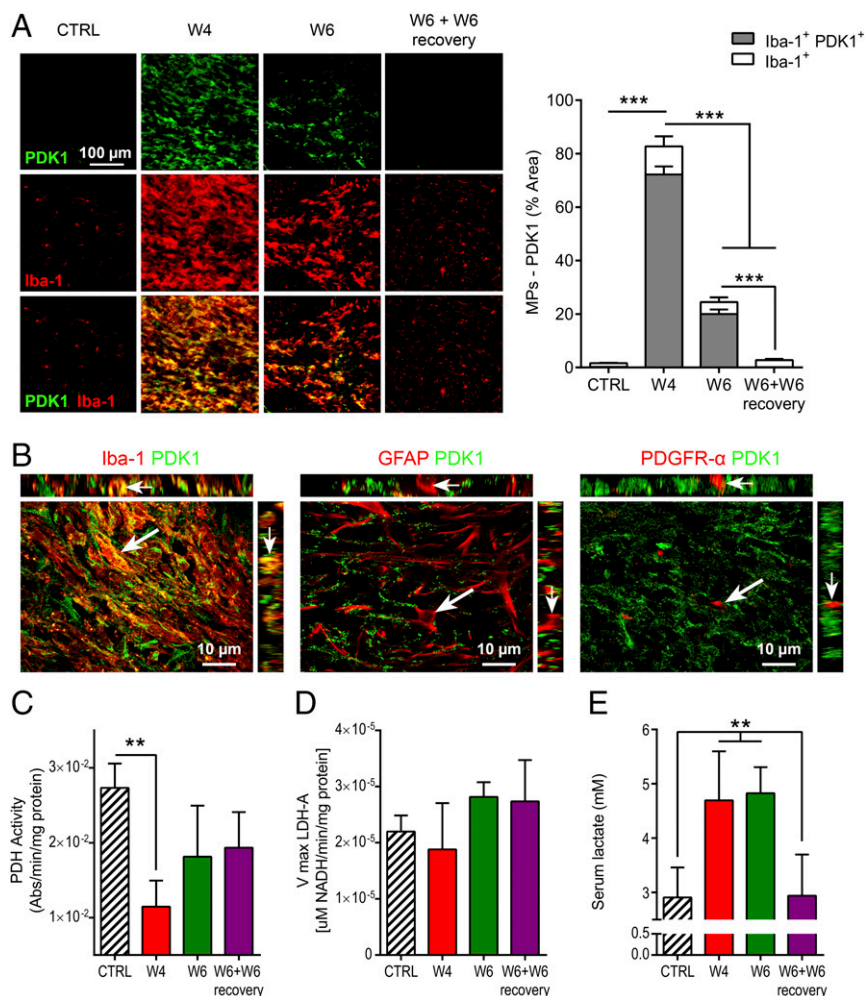
Fig. 4. Increased HP [1-^{13}C]lactate production is associated with up-regulation of PDK1 in activated MPs and decreased PDH activity in the corpus callosum. (*A*) Immunofluorescence staining for PDK1 (green) and MPs (Iba-1, red) reveal overexpression of PDK1 in MPs after W4 of CPZ diet (yellow). Quantitative analyses confirmed the significant up-regulation of PDK1 after W4 of CPZ ($P < 0.0001$), ($n = 3$ mice per time point). (Scale bar: 100 μm.) (*B*) Confocal microscopy confirmed cellular colocalization (yellow, arrows) of PDK1 (green) in MPs (Iba-1, red) at W4 of CPZ diet. In contrast, astrocytes (GFAP, red, arrow) and OPCs (PDGFR-α, red, arrow) staining did not colocalize with PDK1 staining (green) at W4 of CPZ diet, as shown by confocal microscopy. (Scale bar: 10 μm.) (*C*) Quantitative analyses revealed a significant decrease of PDH enzyme activity at W4 of CPZ diet ($P = 0.0026$) and (*D*) no significant change in LDH-A enzyme activity (reported as V_{max}). (*E*) Serum lactate levels were significantly increased at W4 and W6 of CPZ diet (161 ± 62% W4 $P = 0.0014$; 166 ± 48% W6 $P = 0.0007$) and returned to CTRL levels by the end of the recovery period ($P = 0.0024$), ($n = 4$–6 mice per time point). All values are reported as mean ± SD (one-way ANOVA, Tukey HSD post hoc test **$P < 0.01$, ***$P < 0.001$).

microglial activation HP [1-^{13}C]lactate levels were not increased, suggesting a central role for MPs in the detected HP signal. We further showed that, at W4 in the nontransgenic model, the majority of activated MPs present in the corpus callosum overexpressed PDK1 and that PDH activity was significantly decreased in this region, providing a plausible mechanism for the observed increased HP [1-^{13}C]lactate levels.

We opted to investigate the well-established CPZ mouse model for MS, whose strengths lie in the localization of the lesions, their well-known pathogenesis, and their reproducibility in time and space, allowing for longitudinal validation of imaging methods (37, 47, 48). In this model, the vast majority of activated MPs are endogenous microglia, not peripheral macrophages (49–52). At W4 of CPZ, proinflammatory MPs in the corpus callosum express the phagocytic marker CD11b and are responsible for the phagocytosis of myelin debris (53, 54). This supportive action of MPs is an essential step for subsequent remyelination at W6 and W6 + W6 recovery (49, 55). Indeed, directing MPs toward an antiinflammatory phenotype before and during the first weeks of CPZ diet prevents in part oligodendrocyte cell death, demyelination, and

astrogliosis (52, 56). We chose to monitor CPZ mice at W4 and W6 of CPZ diet and after a subsequent period of 6 wk without CPZ because these three time points are characterized by different cellular events. At W4 of CPZ diet, cerebral lesions show a large recruitment and proliferation of MPs, which induce demyelination and can reach up to 50 times the density of microglia present under normal conditions (40). By W6 of CPZ diet, most of the MPs have disappeared and remyelination is ongoing despite continuous administration of the toxin (57, 58). After the 6-wk recovery period, remyelination has occurred, MP number has returned to baseline, and only astrogliosis remains. These marked differences between the cellular events happening at W4, W6, and W6 + W6 recovery justifies the longitudinal follow-up of CPZ mice at these three time points and enabled us to evaluate the potential of ^{13}C MRSI of HP [1-^{13}C]pyruvate to detect the presence of proinflammatory MPs.

Current clinical evaluation of MS brain lesions essentially includes conventional T$_2$-weighted and gadolinium-enhanced T$_1$-weighted MRI (59, 60). Although these methods provide high spatial sensitivity, prediction of outcome and response to treatment remains challenging. Gadolinium-enhanced T$_1$ lesions
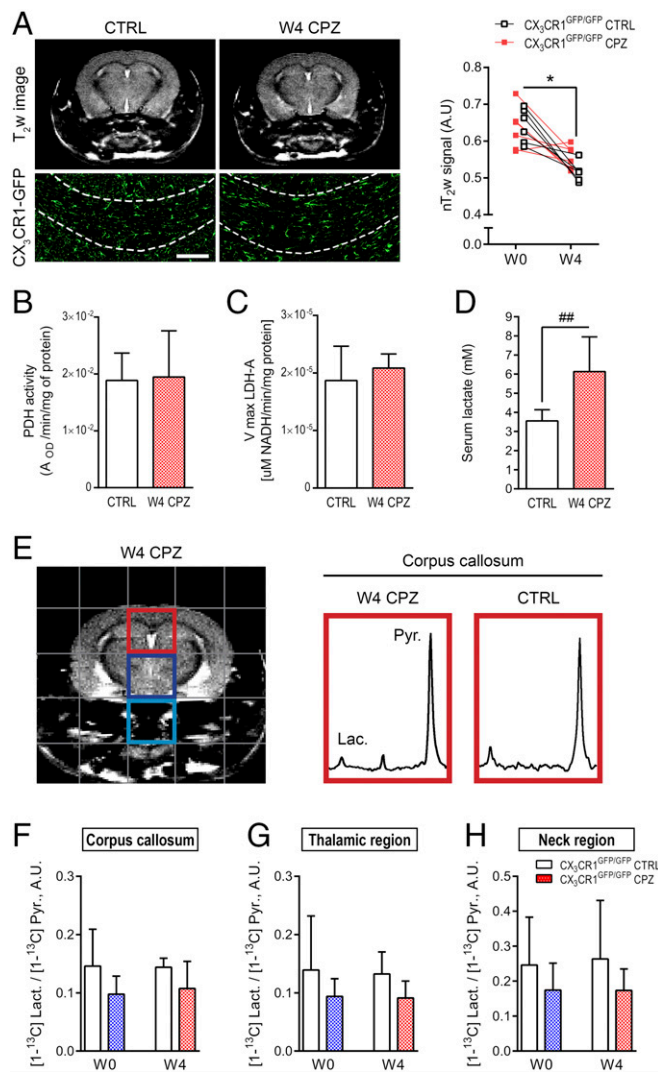
Fig. 5. HP [1-^{13}C]lactate levels are not increased in the corpus callosum of CX$_3$CR1$^{GFP/GFP}$ transgenic mice harboring microglial activation deficiency, suggesting a central role of MPs to the detected HP [1-^{13}C]lactate signal. (*A*) T$_2$-weighted MRI of CX$_3$CR1$^{GFP/GFP}$ mice show similar hypointense contrast of the corpus callosum regardless of diet (CTRL or W4 CPZ). nT$_2$w were significantly decreased at W4 in CPZ and CTRL CX$_3$CR1$^{GFP/GFP}$, reflecting normal myelination ($P \leq 0.0171$). Immunofluorescence images of CX$_3$CR1$^{GFP/GFP}$ microglia show no evident microgliosis in the corpus callosum of CX$_3$CR1$^{GFP/GFP}$ mice despite the CPZ diet. (Scale bar: 100 μm.) (*B*) PDH and (*C*) LDH-A activities from the corpus callosum were not significantly different between CPZ and CTRL groups. (*D*) Serum lactate levels were significantly increased following W4 CPZ, in line with a systemic toxic effect of CPZ diet (173 ± 79%, $P = 0.0079$). (*E*) T$_2$-weighted image overlaid with the HP ^{13}C grid is shown for a W4 CPZ CX$_3$CR1$^{GFP/GFP}$ mouse. HP ^{13}C spectra for CTRL and W4 CPZ CX$_3$CR1$^{GFP/GFP}$ mice show no evident differences between CTRL and CPZ groups in any studied voxel (corpus callosum red; thalamic region dark blue; neck voxel light blue). HP [1-^{13}C]lactate-to-pyruvate ratios for (*F*) the corpus callosum, (*G*) the thalamic area, and (*H*) the neck were not significantly different between CTRL and CPZ groups at any time points ($n = 5$–7 mice per group). All values are reported as mean ± SD (two-way ANOVA, Tukey HSD post hoc test *$P < 0.05$; unpaired t test ##$P < 0.01$). A.U., arbitrary unit; Lac, lactate; Pyr, pyruvate.

noninvasive methods for assessment of neuroinflammatory status in chronic, nonenhancing lesions in gray and white matter are still lacking. Such limitations represent a major drawback for evaluation of lesion formation and monitoring of regenerative and antiinflammatory therapies. In this study we showed that, whereas T$_1$-weighted postcontrast MRI confirmed the lack of BBB breakdown in the CPZ model, nT$_2$w values enabled the detection of CPZ-induced lesions and long-lasting changes associated with a demyelinating event. However, this measure could not readily distinguish between lesion stages linked to different underlying cellular events, notably acute inflammation at W4 CPZ. In contrast, using ^{13}C MRSI of HP [1-^{13}C]pyruvate, we were able to detect an increase of HP [1-^{13}C]lactate production specifically at W4 CPZ in lesions presenting a high level of proinflammatory MPs, thus highlighting the potential added value of this metabolic imaging strategy compared with conventional MR methods.

Following i.v. injection, we detected delivery of HP [1-^{13}C]pyruvate in the corpus callosum of CTRL and CPZ mice. Interestingly, levels of HP [1-^{13}C]pyruvate were comparable between these two groups for all time points. This result is in line with the fact that, unlike in the EAE model, the induction of lesions following CPZ diet occurs without BBB disruption (49–51, 58, 63). Furthermore, and importantly, we were able to detect production of HP [1-^{13}C]lactate from HP [1-^{13}C]pyruvate in the corpus callosum of both CTRL and CPZ animals and a significant increase in HP [1-^{13}C]lactate production at W4 in the CPZ group only. In agreement with other HP ^{13}C MRSI
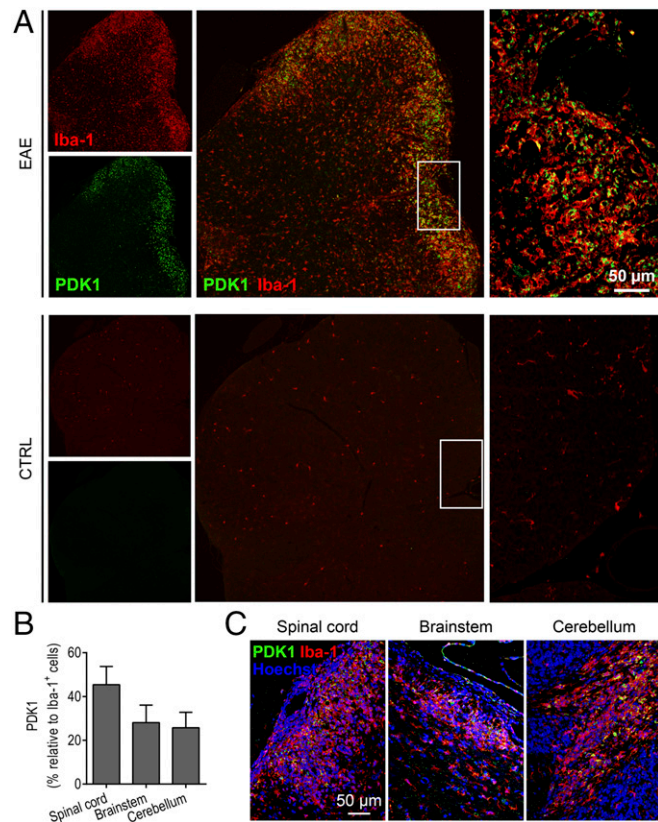

Fig. 6. Detection of PDK1-expressing MPs after EAE induction. (*A*) Immunofluorescence staining for MPs (Iba-1, red) shows increased number of MPs and expression of PDK1 (green) in the spinal cord 30 d after EAE induction compared with age- and sex-matched CTRL. (*B* and *C*) Quantitative analyses reveal that 45 ± 8% of MPs present in the lesions coexpress Iba-1 and PDK1 (yellow) in the spinal cord, 28 ± 8% in the brainstem, and 26 ± 7% in the cerebellum, whereas the level of PDK1 in the CTRL group was below detection. All values are reported as mean ± SD ($n = 3$ mice).

are indicative of altered blood–brain barrier (BBB) and are considered the main radiologic marker of active MS lesions (59, 61). However, whereas density of active lesions are linked to treatment efficacy in some cases, formation of new T$_1$ lesions may occur subclinically and thus more frequently than clinical relapses, limiting treatment monitoring (62). Furthermore,

studies (32), this result suggests that, even in the presence of an intact BBB, enough HP [1-^{13}C]pyruvate enters the brain for the conversion of HP [1-^{13}C]pyruvate to lactate and its variations with disease progression to be detected during the time frame of an experiment.

To assess whether changes in endogenous lactate levels and/or vascular changes contributed to the increased HP [1-^{13}C]lactate signal observed, through label exchange into the lactate pool (32, 64), we performed T$_1$-weighted MRI and serum lactate level analysis. T$_1$-weighted MRI postcontrast showed comparable kinetics of signal enhancement in the corpus callosum of CTRL and CPZ animals at W4, suggesting that global vascular changes (blood flow, permeability, and perfusion) are unlikely to be the driving mechanisms behind the detected increase in HP [1-^{13}C]lactate production observed at that time point. Regarding lactate levels, our results show that serum lactate levels are significantly increased following W4 of CPZ diet, in both nontransgenic and CX$_3$CR1$^{GFP/GFP}$ animals. Importantly, however, only in the nontransgenic animals presenting a high density of MPs in the corpus callosum did the HP [1-^{13}C]lactate significantly increase at W4. Furthermore, this increase was specific to the corpus callosum of the nontransgenic mice only and was not observed in thalamus or in the neck voxel containing blood vessels in any of the two models. Finally, albeit increased compared with CTRL, serum lactate levels in nontransgenic CPZ animals were highly comparable between W4 and W6 of CPZ diet ($P = 0.986$), whereas HP [1-^{13}C]lactate signal in the corpus callosum was only increased at W4 and not at W6. Altogether, these data strongly support the fact that MP proliferation in the corpus callosum at W4 is likely responsible for the increased HP [1-^{13}C]lactate signal seen in the DNP experiments. However, one cannot rule out the fact that inflammation-related increases in the flow of blood containing ^{13}C-labeled lactate rather than metabolic processes within MPs can contribute to the detected changes in HP [1-^{13}C]lactate, because post-Gd T$_1$-weighted MR data cannot rule out this possibility. Additionally, some contribution of endogenous brain lactate (e.g., from necrotic regions), albeit unlikely, cannot be ruled out.

We showed that MPs, astrocytes, and OPCs were modulated by CPZ diet in the corpus callosum of nontransgenic mice, with a dramatic 50-fold increase in MP density in this region at W4. We also demonstrated that only proinflammatory MPs up-regulate the enzyme PDK1, whereas astrocytes and OPCs did not. This result, combined with the lower levels of OPCs and the different temporal evolution of astrogliosis (maximum at W6), highly suggest that PDK1+ MPs are the major cell type contributing to the increased HP [1-^{13}C]lactate at W4 (40). Interestingly, we found a global decrease of PDH activity in the corpus callosum of nontransgenic CPZ mice at W4, but not in the thalamus, whereas LDH-A activity in both regions was unchanged by CPZ diet. In transgenic CX$_3$CR1$^{GFP/GFP}$ animals with low microglial activation both PDH and LDH-A were unchanged in the corpus callosum. These findings provide a plausible explanation for the increased HP [1-^{13}C]lactate observed at W4 of CPZ diet in nontransgenic mice only, with low PDH activity preventing the entrance of pyruvate into the Krebs cycle and redirecting HP [1-^{13}C]pyruvate toward HP [1-^{13}C]lactate production. These results also suggest that the underlying mechanism of increased HP [1-^{13}C]lactate production linked to inflammation is different from the one observed in cancer, in which LDH-A overexpression is the most common player (32, 65). Future studies performed in in vitro controlled systems (e.g., MP cell cultures) are now needed to fully confirm the link between PDK1 up-regulation, PDH activity, and increased lactate production. Nonetheless, our results are in line with recent studies (13, 16) and provide a strong rationale for the observed increase in HP [1-^{13}C]lactate. We additionally showed the expression of PDK1 in MPs in EAE-induced inflammatory and demyelinated spinal cord lesions (Fig. 6), suggesting that PDK1 up-regulation is a commonly shared feature of proinflammatory MPs that is conserved among different neuroinflammation models.

From a technical perspective, we evaluated the dynamic conversion of HP [1-^{13}C]pyruvate into lactate by acquiring spectra every 3 s for a period of a minute. This achievement comes with the trade-off of a lower spatial resolution, which may result in lower sensitivity to subtle lactate changes. For instance, after W6 of CPZ administration we observed a strong reduction of MPs in the corpus callosum. Although most of the remaining MPs still express PDK1 and there is a trend toward decreased PDH activity compared with CTRL, we did not detect a significantly increased production of HP [1-^{13}C]lactate at that time point, which may be explained by the limited sensitivity of HP ^{13}C MRSI to lower MP number. Furthermore, the lack of increase in the HP [1-^{13}C]lactate-to-pyruvate ratios in two of seven mice at W4 (Fig. 2D), despite the likely infiltration of MPs in these animals, should be acknowledged as a probable technical failure of the DNP methodology. Future improvements in hardware and MR acquisition schemes will likely help in reaching a higher sensitivity/specificity and improve the detection of smaller lesions.

In conclusion, this paper shows that metabolic imaging using HP ^{13}C MRSI can be used to monitor neuroinflammatory lesions noninvasively in a preclinical model for MS. Increase in HP [1-^{13}C]lactate production can be detected in cerebral lesions and is associated with high levels of PDK1+-activated MPs and subsequent regional PDH inhibition. Altogether, our results demonstrate a potential for ^{13}C MRSI of HP [1-^{13}C]pyruvate as a neuroimaging method for assessment of inflammatory lesions. Because HP ^{13}C MRSI is clinically translatable (33) and expanding rapidly, this study is of high significance for future clinical trials not only on MS but also all neurological diseases presenting an inflammatory component (66). When used in conjunction with conventional MRI techniques, such a method would enhance diagnosis and help refine therapeutic regimens, which will ultimately improve clinical outcome and patient care.

Materials and Methods

Animals and Experimental Outline. All animal research was approved by the Institutional Animal Care and Use Committee of the University of California, San Francisco. For CPZ studies, 8-wk-old B6(Cg)-*Tyr*$^{c-2J}$/J (stock no. 000058) albino female mice and 8-wk-old B6.129P-*Cx3cr1*^{tm1Litt}/J (stock no. 005582) mice (referred to above as CX$_3$CR1$^{GFP/GFP}$) were purchased from Jackson Laboratories. Mice [$n = 43$ B6(Cg)-*Tyr*$^{c-2J}$/J; $n = 6$ *Cx3cr1*^{tm1Litt}/J] received a 0.2% wt/wt CPZ (Sigma-Aldrich) diet for up to 6 wk. Age-matched CTRL mice received a standard rodent chow [$n = 22$ B6(Cg)-*Tyr*$^{c-2J}$/J; $n = 6$ *Cx3cr1*^{tm1Litt}/J]. For B6(Cg)-*Tyr*$^{c-2J}$/J mice, a subset of animals were imaged longitudinally prior (W0), and after 4 and 6 wk of CPZ (W4 and W6) as well as after 6 wk of CPZ followed by 6 wk of standard rodent chow (W6 + W6 recovery) ($n = 7$ CPZ and 7 CTRL). For *Cx3cr1*^{tm1Litt}/J animals, all mice were imaged at W0 and W4 ($n = 6$ CPZ and 6 CTRL). For immunofluorescence staining, enzyme activity assays, and serum lactate levels, a subset of mice was killed at each time point ($n = 3$–6 CTRL, 3–6 W4, 3–6 W6, and 3–6 W6 + W6 recovery). For EAE induction, 8-wk-old C57BL/6J female mice were injected s.c. with 100 μg of myelin oligodendrocyte glycoprotein (MOG$_{35-55}$), in complete Freund's adjuvant (Difco Laboratories) (67). After immunization and 2 d later mice received 400 ng of pertussis toxin i.p. At 30 d postinjection mice ($n = 3$ EAE and 3 age-matched CTRL) were killed and CNS tissue was collected. For all experiments animals were observed daily, and clinical signs were assessed as follows: 0, no signs; 1, decreased tail tone; 2, mild monoparesis or paraparesis; 3, severe paraparesis; 4, paraplegia; 5, quadraparesis; and 6, moribund or death. Mice with an EAE score of 2.5 ± 0.5 at 30 days postinjection were used for the experiments.

In Vivo MR Acquisitions. All in vivo MR experiments were conducted on a 14.1 T vertical MR system (Agilent Technologies) equipped with 100 G/cm gradients and a dual tune ^{1}H-^{13}C volume coil (Ø$_i$ = 40 mm). For each imaging session, mice were anesthetized using isoflurane (1–3% in O$_2$) and a 27-gauge catheter was secured in the tail vein to allow for i.v. injection of the HP probe. Animals were placed in a dedicated cylindrical cradle allowing for reproducible positioning of the mouse head; the cradle was then tightly inserted inside the volume coil, which was secured to the MR bore to ensure similar positioning between experiments. Respiration and temperature were continuously monitored to ensure animal well-being and data reproducibility.

T$_2$-weighted MRI was acquired using the following parameters: TE/TR = 20/1,200 ms, slice thickness = 0.5 mm, number of averages = 2, matrix = 256 × 256, and field of view (FOV) = 30 × 30 mm^2. For HP ^{13}C MRSI acquisitions, 24 μL

of [1-^{13}C]pyruvate preparation was hyperpolarized using a Hypersense DNP polarizer (Oxford Instruments) for 1 h (29). Note that all pyruvate preparations used in this study were prepared as large batches and underwent quality control to ensure reproducible polarization level between experiments (10–12%). After dissolution, HP [1-^{13}C]pyruvate was rapidly dissolved in isotonic buffer (pH ~7) to a final concentration of 80 mM. A final volume of 300 μL of the solution was then injected i.v. over 12 s through the tail vein catheter. From the beginning of the iv injection, 2D dynamic chemical shift imaging (CSI) ^{13}C data were acquired using the following parameters: TE/TR = 1.2/60 ms; spectral width = 2,500 Hz; 128 points; flip angle (FA) = 10°; FOV = 24 × 24 mm^2; matrix 8 × 8 × 8; in-plane resolution 3 × 3 mm^2; 5-mm slice thickness; scan time 3 s per time point; and 16 time points (68).

T$_1$-weighted images (TE/TR = 1.14/39 ms, FA = 40°, 10 slices, thickness = 1.5 mm, NA = 1, matrix = 128 × 128, and FOV = 22.4 × 22.4 mm^2) were acquired prior (five images) and after (25 images) i.v. injection of Magnevist (gadopentetate dimeglumine, gadolinium-based contrast agent, 1 mmol/kg).

MR Data Analysis. The corpus callosum was defined as the region of interest and manually delineated on the T$_2$-weighted images according to the Franklin and Paxinos anatomical mouse brain atlas (69) with AMIRA software (Mercury Computer Systems). The average signals from the corpus callosum were normalized to the mean cerebrospinal fluid signal of the third ventricle as signal value standard. In a similar manner, the corpus callosum and the thalamus were delineated on T$_1$-weighted images and simple kinetic parameters of contrast enhancement (area under the curve, slope, and relative signal enhancement ([(MR signal postcontrast − MR signal precontrast)/MR signal precontrast]*100) were calculated, as surrogate values of global perfusion, permeability, and blood flow, as previously described (70, 71).

HP ^{13}C MRSI datasets were analyzed using the in-house SIVIC software (https://sourceforge.net/apps/trac/sivic/) and custom-built programs written in MATLAB (MATLAB R2011b; The MathWorks Inc.). HP [1-^{13}C]lactate and HP [1-^{13}C]pyruvate levels were calculated as the sum of integrals over time and normalized to noise level (Fig. S1). Color heat maps of HP [1-^{13}C]lactate-to-pyruvate ratio were generated using a sinc-based interpolation of the ^{13}C 2D CSI data to the resolution of the anatomical images using custom-built programs written in MATLAB and SIVIC.

Immunofluorescence Acquisition and Analysis. All analyses were performed according to previously described procedures (72). Mice were first perfused with an ice-cold 0.9% NaCl solution followed by an ice-cold 4% paraformaldehyde (PFA) solution. Next, brains were dissected and further fixed in 4% PFA for 2 h then dehydrated through a sucrose gradient (2 h at 5%, 2 h at 10%, and overnight at 20%). Afterward, brain tissue was snap-frozen in liquid nitrogen and kept at −80 °C until further processing. Ten-micrometer-thick cryosections were collected. Immunofluorescence staining was performed on brain slides using the following antibody combinations: a primary chicken anti-myelin basic protein (MBP) antibody (AB9348; 1:200 dilution; Millipore) with a secondary donkey anti-chicken DyLight 549 antibody (703-506-155, 1:1,000 dilution; Jackson); a primary rabbit anti-Iba-1 antibody (019-19741, 1:500 dilution; Wako) with a secondary donkey anti-rabbit Alexa Fluor 555 (A31572, 1:1,000 dilution; Invitrogen); a primary mouse anti-PDK1 antibody (AB110025, 1:100 dilution; Abcam) with a secondary goat anti-mouse Alexa Fluor 488 (A11017, 1:100 dilution; Invitrogen); a primary rabbit anti-GFAP (AB7779, 1:500 dilution; Abcam) with a secondary goat anti-rabbit Alexa Fluor 488 (A11008, 1:1,000 dilution; Invitrogen) or with a secondary donkey anti-rabbit Alexa Fluor 555 (A31572, 1:1,000 dilution; Invitrogen); and a primary rat anti-mouse CD140a PDGFR-α (clone APA5, 1:500 dilution; BD Pharmigen) with a secondary goat anti-rat 570 Fab (1:50, 112–297-003; Jackson ImmunoResearch). Slides were counterstained using Hoechst 33342 (H3570, 1:2,000 dilution; Invitrogen). Following staining, sections were mounted using Prolong Gold Antifade (P36930; Invitrogen). Fluorescence image acquisition was performed using an inverted microscope (Ti-E; Nikon). The custom-built epi-illumination optics includes excitation lasers at 405 nm (for DAPI), 488 nm (for eGFP), 561 nm (for mCherry), and 642 nm (For Cy5). The images were recorded with an EMCCD camera (iXon+ DU897E-CS0-BV; Andor). The microscope was controlled using custom software written in Python. Quantitative analyses of immunofluorescence images were performed using NIH ImageJ (v1.46r). The levels of microglia/macrophages (Iba-1), astrocytes (GFAP), OPCs (PDGFR-α), PDK1, and myelin (MBP) were determined based on the image-covering staining and expressed as percentage of the total area (39, 40). For confocal microscopy, images were acquired using a Zeiss LSM780 controlled by Zen software (Zeiss 2014). Only linear adjustments were made during image acquisition.

Spectrophotometric Assay. A subset of mice were killed at each time point of interest [W0 (CTRL), W4, W6, and W6 + W6 recovery] and brains were rapidly dissected. The corpus callosum was then isolated and snap-frozen and samples were stored at −80 °C until further processing. The enzymatic activity of PDH was assessed using spectrophotometric activity assay kit (ab109902; Abcam), according to manufacturer's guidelines and normalized to the concentration of protein determined by the Bradford method (n = 4–6 mice per group). The enzymatic activity of LDH-A (V_{max}) was assessed as previously shown (73) (n = 4–6 mice per group).

Serum Lactate Levels. A subset of mice was anesthetized at each time point [W0 (CTRL), W4, W6, and W6 + W6 recovery] and blood was collected through the tail vein. Serum lactate levels were measured using an assay kit (L-lactate assay kit, colorimetric, ab65331; Abcam) (n = 4–6 mice per group).

Statistical Analysis. For all experiments sample sizes were determined based on previous experience of tumor-bearing mice imaging using ^{13}C MRSI of HP [1-^{13}C]pyruvate at 14.1 T (32, 68). Based on this experience, we assumed that seven to eight animals per experimental group studied longitudinally would suffice to get significant HP data using a two-way repeated measure ANOVA test with P = 0.05. For immunohistochemistry and activity assays we determined that three to four animals per group would suffice to get significant data using a one-way ANOVA test with P = 0.05. With such group sizes, we would have 80–90% power to detect an effect size of 1.25.

Results are expressed as mean ± SD. Two-Way ANOVA was used to determine statistical significance of T$_2$-w MRI and HP ^{13}C MRSI between CPZ and CTRL groups and P values were corrected for multiple testing using the Tukey honest significant difference (HSD) post hoc test (*P < 0.05, **P < 0.01, ***P < 0.001). To compare nonlongitudinal data between W6 + W6 recovery and all other time points (W0, W4, and W6) unpaired t test was used (#P < 0.05, ##P < 0.01, ###P < 0.001). Additionally, a repeated measures ANOVA, with P values corrected for multiple testing using the Tukey HSD post hoc test, was used to evaluate a statistical significance in the CTRL group (†P < 0.05, ††P < 0.01, †††P < 0.001). Statistical analyses of immunofluorescence, enzyme activity assays, and serum lactate levels between W0, W4, W6, and W6 + W6 recovery were performed using a one-way ANOVA, and the given P values were corrected for multiple testing using the Tukey HSD post hoc test (*P < 0.05, **P < 0.01, ***P < 0.001, ****P < 0.0001). To evaluate statistical significance of immunofluorescence, enzyme activity assays and serum lactate levels between CTRL and W4 CPZ groups of CX$_3$CR1$^{GFP/GFP}$ mice we used an unpaired t test (#P < 0.05, ##P < 0.01, ###P < 0.001).

1. Noseworthy JH, Lucchinetti C, Rodriguez M, Weinshenker BG (2000) Multiple sclerosis. *N Engl J Med* 343:938–952.
2. Nylander A, Hafler DA (2012) Multiple sclerosis. *J Clin Invest* 122:1180–1188.
3. Calabrese M, et al. (2015) Exploring the origins of grey matter damage in multiple sclerosis. *Nat Rev Neurosci* 16:147–158.
4. Lucchinetti CF, et al. (2011) Inflammatory cortical demyelination in early multiple sclerosis. *N Engl J Med* 365:2188–2197.
5. Quarles R, Macklin W, Morell P (2005) Myelin formation, structure and biochemistry. *Basic Neurochemistry: Molecular, Cellular and Medical Aspects*, eds Siegel G, Albers RW, Brady S, Price D (Elsevier, New York), pp 51–72.
6. Kettenmann H, Hanisch UK, Noda M, Verkhratsky A (2011) Physiology of microglia. *Physiol Rev* 91:461–553.
7. Wang P, Xie K, Wang C, Bi J (2014) Oxidative stress induced by lipid peroxidation is related with inflammation of demyelination and neurodegeneration in multiple sclerosis. *Eur Neurol* 72:249–254.
8. Haider L (2015) Inflammation, iron, energy failure, and oxidative stress in the pathogenesis of multiple sclerosis. *Oxid Med Cell Longev* 2015:725370.
9. Galván-Peña S, O'Neill LA (2014) Metabolic reprograming in macrophage polarization. *Front Immunol* 5:420.
10. Orihuela R, McPherson CA, Harry GJ (2016) Microglial M1/M2 polarization and metabolic states. *Br J Pharmacol* 173:649–665.
11. Tannahill GM, Iraci N, Gaude E, Frezza C, Pluchino S (2015) Metabolic reprograming of mononuclear phagocytes in progressive multiple sclerosis. *Front Immunol* 6:106.
12. Jha MK, et al. (2015) Metabolic connection of inflammatory pain: Pivotal role of a pyruvate dehydrogenase kinase-pyruvate dehydrogenase-lactic acid axis. *J Neurosci* 35:14353–14369.
13. Meiser J, et al. (2016) Pro-inflammatory macrophages sustain pyruvate oxidation through pyruvate dehydrogenase for the synthesis of itaconate and to enable cytokine expression. *J Biol Chem* 291:3932–3946.

14. Kelly B, O'Neill LA (2015) Metabolic reprogramming in macrophages and dendritic cells in innate immunity. *Cell Res* 25:771–784.

15. Vander Heiden MG, Cantley LC, Thompson CB (2009) Understanding the Warburg effect: The metabolic requirements of cell proliferation. *Science* 324:1029–1033.

16. Tan Z, et al. (2015) Pyruvate dehydrogenase kinase 1 participates in macrophage polarization via regulating glucose metabolism. *J Immunol* 194:6082–6089.

17. Jha MK, Jeon S, Suk K (2012) Pyruvate dehydrogenase kinases in the nervous system: Their principal functions in neuronal-glial metabolic interaction and neuro-metabolic disorders. *Curr Neuropharmacol* 10:393–403.

18. Zhang S, Hulver MW, McMillan RP, Cline MA, Gilbert ER (2014) The pivotal role of pyruvate dehydrogenase kinases in metabolic flexibility. *Nutr Metab (Lond)* 11:10.

19. Paling D, Golay X, Wheeler-Kingshott C, Kapoor R, Miller D (2011) Energy failure in multiple sclerosis and its investigation using MR techniques. *J Neurol* 258:2113–2127.

20. Simone IL, et al. (2001) Axonal damage in multiple sclerosis plaques: A combined magnetic resonance imaging and 1H-magnetic resonance spectroscopy study. *J Neurol Sci* 182:143–150.

21. Simone IL, et al. (1996) High resolution proton MR spectroscopy of cerebrospinal fluid in MS patients. Comparison with biochemical changes in demyelinating plaques. *J Neurol Sci* 144:182–190.

22. Nicoli F, et al. (1996) Cerebrospinal fluid metabolic profiles in multiple sclerosis and degenerative dementias obtained by high resolution proton magnetic resonance spectroscopy. *C R Acad Sci III* 319:623–631.

23. De Stefano N, Filippi M (2007) MR spectroscopy in multiple sclerosis. *J Neuroimaging* 17(Suppl 1):31S–35S.

24. Narayana PA (2005) Magnetic resonance spectroscopy in the monitoring of multiple sclerosis. *J Neuroimaging* 15(4 Suppl):46S–57S.

25. Ardenkjaer-Larsen JH, et al. (2003) Increase in signal-to-noise ratio of > 10,000 times in liquid-state NMR. *Proc Natl Acad Sci USA* 100:10158–10163.

26. Brindle KM, Bohndiek SE, Gallagher FA, Kettunen MI (2011) Tumor imaging using hyperpolarized 13C magnetic resonance spectroscopy. *Magn Reson Med* 66:505–519.

27. Chaumeil MM, et al. (2013) Non-invasive in vivo assessment of IDH1 mutational status in glioma. *Nat Commun* 4:2429.

28. Chaumeil MM, et al. (2012) Hyperpolarized 13C MR spectroscopic imaging can be used to monitor everolimus treatment in vivo in an orthotopic rodent model of glioblastoma. *Neuroimage* 59:193–201.

29. Kurhanewicz J, et al. (2011) Analysis of cancer metabolism by imaging hyperpolarized nuclei: Prospects for translation to clinical research. *Neoplasia* 13:81–97.

30. Chaumeil MM, et al. (2014) Hyperpolarized [1-13C] glutamate: A metabolic imaging biomarker of IDH1 mutational status in glioma. *Cancer Res* 74:4247–4257.

31. Keshari KR, Wilson DM (2014) Chemistry and biochemistry of 13C hyperpolarized magnetic resonance using dynamic nuclear polarization. *Chem Soc Rev* 43:1627–1659.

32. Chaumeil MM, Najac C, Ronen SM (2015) Studies of metabolism using (13)C MRS of hyperpolarized probes. *Methods Enzymol* 561:1–71.

33. Nelson SJ, et al. (2013) Metabolic imaging of patients with prostate cancer using hyperpolarized [1-^{13}C]pyruvate. *Sci Transl Med* 5:198ra108.

34. Thind K, et al. (2014) Mapping metabolic changes associated with early radiation induced lung injury post conformal radiotherapy using hyperpolarized (1)(3)C-pyruvate magnetic resonance spectroscopic imaging. *Radiother Oncol* 110:317–322.

35. MacKenzie JD, et al. (2011) Detection of inflammatory arthritis by using hyperpolarized 13C-pyruvate with MR imaging and spectroscopy. *Radiology* 259:414–420.

36. Josan S, et al. (2015) Assessing inflammatory liver injury in an acute CCl4 model using dynamic 3D metabolic imaging of hyperpolarized [1-(13)C]pyruvate. *NMR Biomed* 28:1671–1677.

37. Praet J, Guglielmetti C, Berneman Z, Van der Linden A, Ponsaerts P (2014) Cellular and molecular neuropathology of the cuprizone mouse model: Clinical relevance for multiple sclerosis. *Neurosci Biobehav Rev* 47:485–505.

38. Hiremath MM, et al. (1998) Microglial/macrophage accumulation during cuprizone-induced demyelination in C57BL/6 mice. *J Neuroimmunol* 92:38–49.

39. Praet J, et al. (2015) Cuprizone-induced demyelination and demyelination-associated inflammation result in different proton magnetic resonance metabolite spectra. *NMR Biomed* 28:505–513.

40. Guglielmetti C, et al. (2016) Diffusion kurtosis imaging probes cortical alterations and white matter pathology following cuprizone induced demyelination and spontaneous remyelination. *Neuroimage* 125:363–377.

41. Orije J, et al. (2015) Longitudinal monitoring of metabolic alterations in cuprizone mouse model of multiple sclerosis using 1H-magnetic resonance spectroscopy. *Neuroimage* 114:128–135.

42. Guglielmetti C, et al. (2014) Multimodal imaging of subventricular zone neural stem/progenitor cells in the cuprizone mouse model reveals increased neurogenic potential for the olfactory bulb pathway, but no contribution to remyelination of the corpus callosum. *Neuroimage* 86:99–110.

43. Sturrock RR (1980) Myelination of the mouse corpus callosum. *Neuropathol Appl Neurobiol* 6:415–420.

44. Suzuki K (1969) Giant hepatic mitochondria: Production in mice fed with cuprizone. *Science* 163:81–82.

45. Petronilli V, Zoratti M (1990) A characterization of cuprizone-induced giant mouse liver mitochondria. *J Bioenerg Biomembr* 22:663–677.

46. Wolf Y, Yona S, Kim KW, Jung S (2013) Microglia, seen from the CX3CR1 angle. *Front Cell Neurosci* 7:26.

47. Thiessen JD, et al. (2013) Quantitative MRI and ultrastructural examination of the cuprizone mouse model of demyelination. *NMR Biomed* 26:1562–1581.

48. Nathoo N, Yong VW, Dunn JF (2014) Understanding disease processes in multiple sclerosis through magnetic resonance imaging studies in animal models. *Neuroimage Clin* 4:743–756.

49. Lampron A, et al. (2015) Inefficient clearance of myelin debris by microglia impairs remyelinating processes. *J Exp Med* 212:481–495.

50. Remington LT, Babcock AA, Zehntner SP, Owens T (2007) Microglial recruitment, activation, and proliferation in response to primary demyelination. *Am J Pathol* 170:1713–1724.

51. Voss EV, et al. (2012) Characterisation of microglia during de- and remyelination: Can they create a repair promoting environment? *Neurobiol Dis* 45:519–528.

52. Le Blon D, et al. (2016) Intracerebral transplantation of interleukin 13-producing mesenchymal stem cells limits microgliosis, oligodendrocyte loss and demyelination in the cuprizone mouse model. *J Neuroinflammation* 13:288.

53. Morell P, et al. (1998) Gene expression in brain during cuprizone-induced de-myelination and remyelination. *Mol Cell Neurosci* 12:220–227.

54. Olah M, et al. (2012) Identification of a microglia phenotype supportive of remyeli-nation. *Glia* 60:306–321.

55. Skripuletz T, et al. (2013) Astrocytes regulate myelin clearance through recruitment of microglia during cuprizone-induced demyelination. *Brain* 136:147–167.

56. Guglielmetti C, et al. (2016) Interleukin-13 immune gene therapy prevents CNS in-flammation and demyelination via alternative activation of microglia and macro-phages. *Glia* 64:2181–2200.

57. Gudi V, et al. (2009) Regional differences between grey and white matter in cupri-zone induced demyelination. *Brain Res* 1283:127–138.

58. Matsushima GK, Morell P (2001) The neurotoxicant, cuprizone, as a model to study demyelination and remyelination in the central nervous system. *Brain Pathol* 11:107–116.

59. Rovira À, et al.; MAGNIMS study group (2015) Evidence-based guidelines: MAGNIMS consensus guidelines on the use of MRI in multiple sclerosis-clinical implementation in the diagnostic process. *Nat Rev Neurol* 11:471–482, and erratum (2015) 11:483.

60. Rovira A, Auger C, Alonso J (2013) Magnetic resonance monitoring of lesion evolution in multiple sclerosis. *Ther Adv Neurol Disord* 6:298–310.

61. Abdoli M, Chakraborty S, MacLean HJ, Freedman MS (2016) The evaluation of MRI diffusion values of active demyelinating lesions in multiple sclerosis. *Mult Scler Relat Disord* 10:97–102.

62. van Munster CE, Uitdehaag BM (2017) Outcome measures in clinical trials for multiple sclerosis. *CNS Drugs* 31:217–236.

63. Arnett HA, et al. (2001) TNF alpha promotes proliferation of oligodendrocyte pro-genitors and remyelination. *Nat Neurosci* 4:1116–1122.

64. Day SE, et al. (2007) Detecting tumor response to treatment using hyperpolarized 13C magnetic resonance imaging and spectroscopy. *Nat Med* 13:1382–1387, and erratum (2007) 13:1521.

65. Warburg O (1956) On the origin of cancer cells. *Science* 123:309–314.

66. Perry VH, Nicoll JA, Holmes C (2010) Microglia in neurodegenerative disease. *Nat Rev Neurol* 6:193–201.

67. Didonna A, Cekanaviciute E, Oksenberg JR, Baranzini SE (2016) Immune cell-specific transcriptional profiling highlights distinct molecular pathways controlled by Tob1 upon experimental autoimmune encephalomyelitis. *Sci Rep* 6:31603.

68. Chaumeil MM, et al. (2016) Hyperpolarized (13)C MR imaging detects no lactate production in mutant IDH1 gliomas: Implications for diagnosis and response moni-toring. *Neuroimage Clin* 12:180–189.

69. Franklin K, Paxinos G (1997) *The Mouse Brain in Stereotaxic Coordinates* (Academic, San Diego), 3rd Ed.

70. Kuhl CK, et al. (1999) Dynamic breast MR imaging: Are signal intensity time course data useful for differential diagnosis of enhancing lesions? *Radiology* 211:101–110.

71. Cuenod CA, Balvay D (2013) Perfusion and vascular permeability: Basic concepts and measurement in DCE-CT and DCE-MRI. *Diagn Interv Imaging* 94:1187–1204.

72. Praet J, et al. (2014) Histological characterization and quantification of cellular events following neural and fibroblast(-like) stem cell grafting in healthy and demyelinated CNS tissue. *Methods Mol Biol* 1213:265–283.

73. Ward CS, et al. (2010) Noninvasive detection of target modulation following phos-phatidylinositol 3-kinase inhibition using hyperpolarized 13C magnetic resonance spectroscopy. *Cancer Res* 70:1296–1305.

NEUROSCIENCE